JOURNAL OF PROPULSION AND POWER
Vol. 16, No. 1, January–February 2000

Regression Rate Behavior of Hybrid Rocket Solid Fuels

Martin J. Chiaverini,* Nadir Serin,† David K. Johnson,‡ Yeu-Cherng Lu,§ Kenneth K. Kuo,¶ and Grant A. Risha**
Pennsylvania State University, University Park, Pennsylvania 16802

An experimental investigation of the regression-rate characteristics of hydroxyl-terminated polybutadiene (HTPB) solid fuel burning with oxygen was conducted using a windowed, slab-geometry hybrid rocket motor. A real-time, x-ray radiography system was used to obtain instantaneous solid-fuel regression rate data at many axial locations. Fuel temperature measurements were made using an array of 25-μm fine-wire embedded thermocouples. The regression rates displayed a strong dependence on axial location near the motor head-end. At lower mass flux levels, thermal radiation was found to significantly influence the regression rates. The regression rates were also affected by the addition of activated aluminum powder. A 20% by weight addition of activated aluminum to HTPB increased the fuel mass flux by 70% over that of pure HTPB. Correlations were developed to relate the regression rate to operating conditions and port geometry for both pure HTPB and for HTPB loaded with certain fractions of activated aluminum. Thermocouple measurements indicated that the fuel surface temperatures for pure HTPB were between 930 and 1190 K. The HTPB activation energy was estimated at 11.5 kcal/mole, suggesting that the overall regression process is governed by physical desorption of high-molecular weight fragments from the fuel surface.

Nomenclature

E_a = activation energy, kcal/mole, see Eq. (3)
G = local mass flux, kg/m^2-s
G_o = oxidizer mass flux, kg/m^2-s, see Eq. (1)
h = port height between fuel slabs, m, see Eq. (1)
p = pressure, MPa, see Eq. (1)
Re_x = Reynolds number
R_u = universal gas constant, kcal/mole-K, see Eq. (3)
r = solid-fuel regression rate, mm/s, see Eq. (1)
T_s = fuel surface temperature, K, see Eq. (3)
x = axial location, m, see Eq. (1)
κ = gas absorption coefficient, (m-MPa)$^{-1}$, see Eq. (1)
$\rho_f r$ = fuel mass flux, g/cm^2-s, see Eq. (3)

Introduction

CLASSICAL hybrid rocket motors employ head-end injection of liquid or gaseous oxidizer through an otherwise inert solid-fuel grain. Because of this design, hybrid rockets possess unique safety and operational advantages over both liquid bipropellant and solid-propellant rockets, which make them very attractive for both military and commercial applications. However, hybrid rocket combustion studies are complicated by the interaction between the solid-fuel regression rate and the aerodynamics of the chemically reacting boundary-layer flow through the fuel grain. The solid-fuel regression rate represents the key parameter in the study of hybrid rocket propulsion. Various models and theories have been developed in the past few decades to explain regression-rate behavior; however, the literature has historically lacked a sufficient amount of realistic empirical regression-rate data with which to validate these models over the range of operating conditions expected for practical hybrid rocket motors. Instantaneous regression-rate data have been especially lacking. In an attempt to provide more data for both model validation and useful engineering correlations, an experimental investigation using a lab-scale hybrid motor was conducted. The study focused on the following objectives: 1) nonintrusive measurement of instantaneous and average solid-fuel regression rates under varying operating conditions including gaseous oxygen (GOX) flux level, motor pressure, and fuel formulation; 2) determination of the solid-fuel surface temperatures and subsurface thermal wave profiles as a function of operating conditions; 3) investigation of the effects of solid-fuel additives on regression behavior; 4) development of empirical correlations relating the regression rate to operating conditions and geometric parameters; and 5) determination of an Arrhenius expression to relate regression rate to surface temperature.

Method of Approach

To conduct test firings under realistic operating conditions similar to those expected in both subscale and full-scale motors, a high-pressure, windowed, slab-geometry motor was designed and is shown in Fig. 1. The main body of the motor was constructed from a single block of stainless steel, and had an overall length of 106.7 cm, a width of 17.8 cm, and a height of 25.4 cm. The top and bottom walls were 7.78 cm thick. The two-dimensional motor accommodated two opposing fuel slabs, 58.4 cm (23 in.) long and 7.6 cm (3 in.) wide. The width of the combustion port was also 7.6 cm wide. The sides of the fuel slabs were prevented from burning by tightly sandwiching them between the removable sidewalls of the motor. Fore and aft graphite inserts were used to prevent the fuel slabs from burning on either end. The front edges of the slabs were chamfered slightly to allow the gaseous oxygen to flow smoothly from the precombustion chamber into the combustion port between the two fuel slabs. The initial port height between the fuel slabs was either 0.95 or 1.25 cm. The slabs were either 4.28 or 4.45 cm thick. Table 1 compares the operating conditions of the motor used in this study with those expected in expendable launch vehicles and large boosters.[1] The test matrix range of the 11-in. JIRAD motor is also indicated.[2] The Pennsylvania State University (PSU) hybrid motor has operating conditions comparable with the other systems.

GOX was employed as the oxidizer for all test firings, and hydroxyl-terminated polybutadiene (HTPB) was used as the baseline solid fuel. The HTPB was prepared by mixing R-45M and Isonate 143L (diisocyanate) under vacuum for 30 min and then pouring the liquid fuel into Teflon®-coated molds for curing. The molds were then placed in a vacuum chamber for an additional 30 min to remove any air bubbles entrained during the pouring process. In several tests, either carbon black powder or ultrafine activated aluminum powder (UFAL) was added to the HTPB during the processing stage. Reference 3 discusses the results of the tests using

Received 6 December 1996; revision received 20 March 1998; accepted for publication 14 December 1998.

*Ph.D. Student; currently Aerospace Engineer, Orbital Technologies Corporation, 1212 Fourier Drive, Madison, WI 53717. Member AIAA.
†Visiting Research Assistant.
‡Research Assistant, 139 Research Building East.
§Research Associate. Member AIAA.
¶Distinguished Professor of Mechanical Engineering, 140 Research Building East. Fellow AIAA.
**Ph.D. Candidate, 139 Research Building East. Member AIAA.

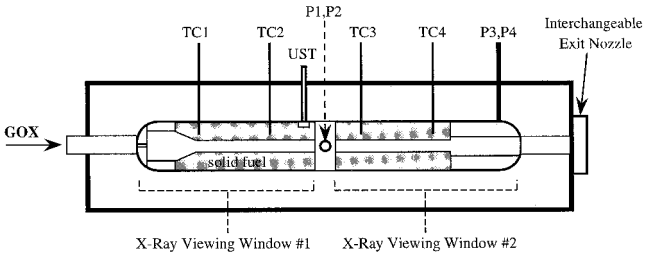

Fig. 1 Schematic diagram of hybrid motor with diagnostic devices.

Table 1 Comparison of hybrid motor operating conditions

Parameter	ELV[a]	Large booster	11-JIRAD	PSU
Pressure, psia	300–600	400–500	145–1009	170–800
G_o, $1b_m/in.^2$-s	0.6–0.8	0.8–1.3	0.14–0.8	0.15–0.65
Initial L/D_h	26–35	32–39	17.6–34	25–37
Average O/F	2.3–2.6	2.5–2.6	1.11–3.33	1.5–2.7

[a]Expendable launch vehicle.

Table 2 Diagnostic techniques used with the hybrid motor

Device	Measurement
Real-time x-ray radiography system	Instantaneous regression rate over a region
Ultrasonic pulse-echo system	Instantaneous regression rate at a single location
Caliper and mass balance	Average regression rate
Fine-write thermocouple array	Fuel surface/subsurface temperature
Microscope	Recovered fuel surface structure
Pressure transducer array	Dynamic/static motor pressures
Critical flow venturi	GOX mass flow rate

carbon black additive as an opacifying agent. The addition of carbon black powder had no noticeable effect on either regression rate or surface temperature. The UFAL powder was added to evaluate its performance as a possible regression-rate enhancing agent and had a mean particle size in the range of 0.05–0.10 μm. It was added in amounts of 4, 12, and 20% of the total fuel weight.

The GOX supply system consisted of a main oxygen feed line and a nitrogen purge line. Eight GOX bottles were manifolded to minimize supply pressure decay during the test firings, which normally lasted 5–10 s. Remotely operated ball valves were used to initiate and terminate the flow of oxygen, whereas a critical flow venturi was used to maintain a steady mass flow of GOX through the main line. The venturi had an adjustable throat area so that the GOX mass flow rate could be easily selected.

Two small, solid-propellant charges located in the precombustion chamber were used to ignite the fuel slabs a few seconds after the start of GOX flow. The solid-propellant sticks were themselves ignited electrically using embedded nichrome wire connected to a 12-V dc power supply. References 4 and 5 provide a more complete description of the entire test rig.

To determine the variables of interest, the motor was instrumented with a number of diagnostic systems, as described in Table 2. Figure 1 shows the approximate locations of four of the seven fine-wire thermocouples (TC), the pressure transducers (P), and the ultrasonic transducer (UST) in the instrumented motor. The 25-μm platinum/platinum-10% rhodium thermocouples were embedded in the fuel samples during casting for measuring the subsurface temperature profiles and burning surface temperatures. Thermocouple ports in the fuel slab support beams were placed at centerline positions corresponding to 6.4, 14.0, 21.6, 29.2, 34.3, 44.5, and 54.6 cm from the leading edge of the fuel slab. Generally, six of the seven ports were used to house thermocouple assemblies, whereas one of the ports was utilized for the ultrasonic transducer feedthrough. For each test, the ultrasonic transducer was positioned either 17.5, 25.1, 33.3, or 40.9 cm downstream from the leading edge of the fuel slab. The ultrasonic pulse-echo system enabled determination of the instantaneous fuel web thickness at one of the four possible axial locations, with a sampling frequency of either 1 or 5 kHz. The electronic device used to control and acquire data from the ultrasonic transducer was obtained from ONERA in France. Only the top fuel slab was instrumented with thermocouples and the ultrasonic transducer.

The x-ray radiography system captured real-time images of the fuel slabs and combustor port over a region about 19 cm long, and therefore provided axial, as well as temporal, variations in the fuel web thickness and regression rate. This radiography system had an overall spatial resolution of 140 μm. As shown in Fig. 1, the assembled motor had two window ports. Because the x-ray radiography system could only view the fuel slabs through one window port at a time, different combinations of windows were used, depending on the location of the x-ray tube head. The x-ray radiography system could not penetrate the steel windows, so that to view the combustion phenomena inside the motor, a transparent Lexan® outer window (19 mm thick) was used in combination with an inner graphite window (13 mm thick) in the two opposing viewing ports accommodating the x-ray radiography system. The Lexan window provided strength, whereas the graphite window provided thermal protection for the outer Lexan window. For the second pair of viewing ports, an outer steel window (19 mm thick) and an inner graphite window (13 mm thick) were used. All windows were 28.0 cm long × 4.35 cm wide. During a test, the x-ray tube head emitted high-energy photons that passed through the Lexan/graphite window assemblies of the motor and then impinged on an image intensifier. Inside the motor, a portion of the x-ray photon energy was absorbed by the solid fuel; however, the photons that passed through the port area between the fuel slabs experience little absorption. Because of this difference in the attenuation of the x-ray photons, the x-ray images displayed contrasting bright and dark regions, which showed the port area and fuel slabs, respectively. The local, instantaneous fuel web thickness and port height were then deduced from these images using image-processing software. The time resolution between consecutive images was about 33.33 ms, whereas web thickness and port height measurements were made at 12.5-mm increments along the fuel slabs. The instantaneous regression rates were obtained by processing the fuel web thickness time histories at each axial station. The procedures used to obtain the instantaneous regression rates will not be discussed here because Ref. 3 provides a thorough treatment of the data-processing routines for both the x-ray radiography and ultrasonic pulse-echo methods. Reference 3 also shows that the regression rates obtained using these two techniques generally agreed within about ±4%. This paper focuses mainly on data obtained from the real-time x-ray radiography system because it provided spatial as well as temporal variations in the regression rate. It is believed that this investigation represents the first application of real-time x-ray radiography for the determination of instantaneous solid-fuel regression rates in a hybrid motor. References 4–7 provide a detailed description of both the ultrasonic pulse-echo and real-time x-ray radiography methods.

Results and Discussion

To investigate HTPB regression-rate behavior, a series of tests was conducted at different GOX mass fluxes and chamber pressure levels with both pure and UFAL-loaded HTPB. Figure 2 shows a typical pressure–time trace from the hybrid motor, indicating pressure oscillations on the order of ±1% of the mean pressure and a pressure drop due to erosion of the graphite exit nozzle. Though the pressure decay is not desirable, the real-time x-ray radiography system allowed direct correlation between the regression rates and other motor operating conditions, including the pressure, in an instantaneous sense. The initiation of GOX flow, at the 1-s mark, causes the initial increase in motor pressure. The GOX flow was terminated at 9 s.

Solid-Fuel Regression Rate Results

Because HTPB fuel has been widely used by various researchers in different hybrid motor studies, it is useful to examine some

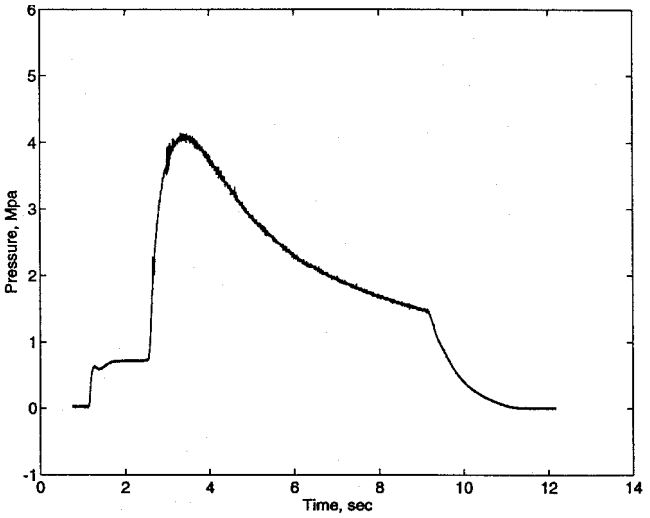

Fig. 2 Typical motor pressure-time trace.

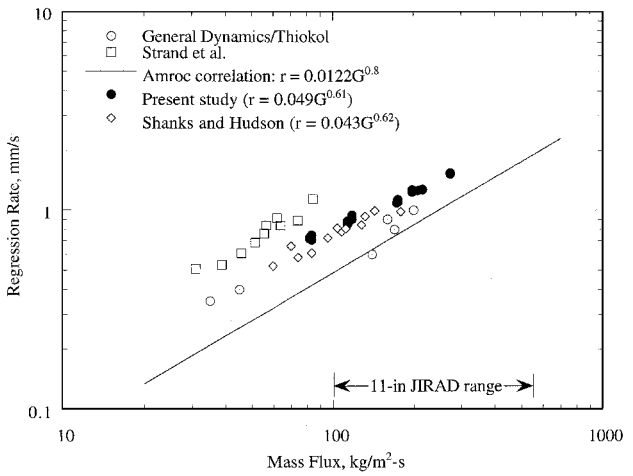

Fig. 3 Comparison of several solid-fuel regression-rate studies.

regression-rate results from the literature. Figure 3 compares the average regression rate r vs local mass flux G trends observed in this study with data obtained by other researchers. Interestingly, the data from the present study, obtained using a slab-geometry motor, match very well with the data of Ref. 8, gathered from experiments using a tube burner. The Amroc correlation and General Dynamics data seem somewhat lower than the other data sets, a difference perhaps caused by scaling effects. Differences among the particular HTPB prepolymer and curing agent may also contribute to discrepancies among the data sets. The mass flux range of the 11-in. diam JIRAD motor is also shown in Fig. 3.

For the present study, r varies with G to the power of 0.61 instead of the theoretical 0.8 for turbulent flow over a flat plate.[9] Shanks and Hudson[8] present a very similar correlation, indicating a power of 0.62. For clarity, these data fits are not shown in Fig. 3. In addition, Sutton[10] showed that r depended on G_o to the 0.681 power for a small-scale tube burner.[10] These findings imply that nonconvective processes, such as radiant heat flux and/or finite rate chemical kinetics, may influence the solid-fuel regression rates in hybrid rocket motors. Note that simple correlations like that shown in Fig. 3 give no indication of how the regression rate varies with other important operating conditions, such as oxidizer-to-fuel ratio and motor pressure, or with geometric parameters such as hydraulic diameter or axial location along the fuel grain.

Internal Ballistic Behavior

Figure 4 shows the regression-rate-time traces at several axial locations for a single test, deduced using the real-time x-ray radiography system. Because of the limited temporal resolution available with this system, no attempt was made to deduce the regression-rate ignition or shutdown transients using x-ray data. However, the ultrasonic pulse-echo method had sampling intervals of about 0.2 ms, and was used to determine the instantaneous regression rate over the entire test from ignition to motor shutdown. These results and subsequent analysis are discussed in Ref. 3.

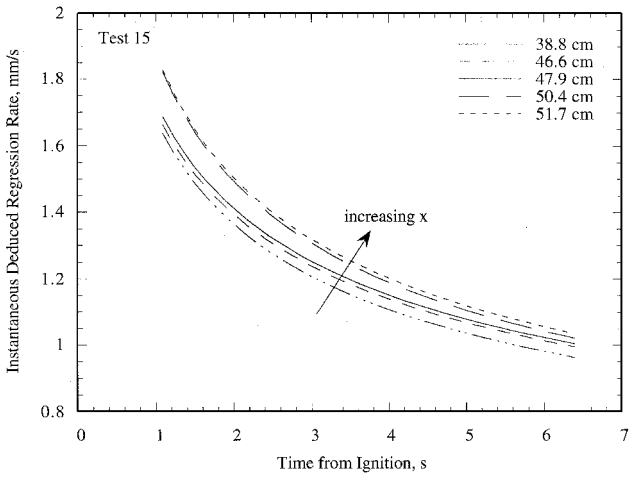

Fig. 4 Representative regression-rate-time traces.

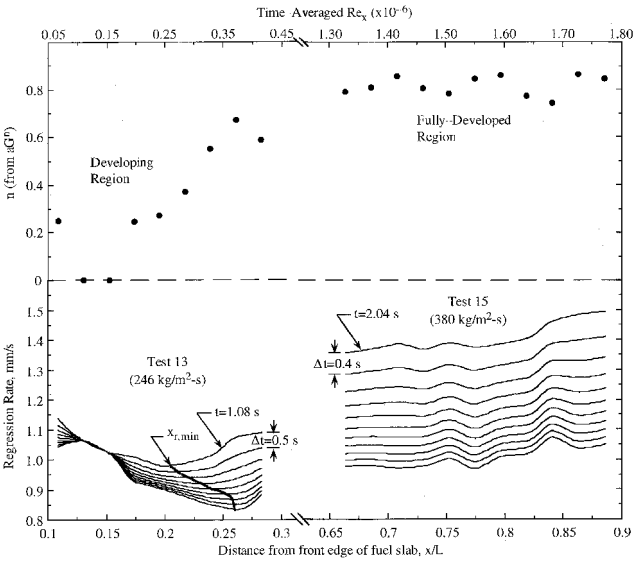

Fig. 5 Internal ballistic behavior.

As shown in Fig. 4, the regression rates are relatively high at the beginning of the test, but decrease continuously with time due to the increase in the local port area and corresponding decrease in the local mass flux, which, for convectively governed solid-fuel regression, is the most influential operating condition. Because local mass flux increases in the downstream direction due to fuel mass addition, the regression rates also tend to increase with axial location measured from the fuel slab leading edge, as indicated in Fig. 4. However, as shown by Marxman and Gilbert,[11] a location of minimum regression rate could exist somewhere on the fuel slab. For optimal fuel-grain design, the prediction of this location may be important.

Figure 5 illustrates the typical solid-fuel internal ballistic behavior observed in this study. The lower portion of the graph shows several instantaneous regression-rate profiles from test 13, with an initial GOX mass flux of 246 kg/m^2-s; and from test 15, with an initial GOX mass flux of 380 kg/m^2-s. The regression-rate profiles are 0.5 s apart for test 13 and 0.4 s apart for test 15. For test 13, the x-ray radiography system was set up to view the upstream portion of the fuel slabs, whereas for test 15, the x-ray images were taken

from the downstream region of the fuel slabs. The break between the two sets of regression-rate profiles is due to obstruction by metal support pieces between the two viewing windows and to the selection of the particular viewing area for each test. The regression rates were higher for test 15 due to both the higher injected GOX mass flux and the higher local mass flux in the downstream sampling location. According to the data, the regression rates are relatively high near the leading edge of the fuel slabs, but decrease with axial location for a certain interval until reaching a minimum, beyond which the regression rates increase with increasing axial distance from the leading edge. It is believed that this point of minimum regression rate corresponds to the crossover of two competing effects: boundary-layer growth, as represented by the local Reynolds number, and increase of the local mass flux. Near the leading edge of the fuel slab, the boundary layer is very thin and has relatively large velocity and temperature gradients, which result in high shear stress and convective heat flux. However, the boundary layer grows in the downstream direction, causing the velocity and temperature gradients, and therefore, the convective heat flux, to decrease. At the same time, the local mass flux increases in the downstream direction due to upstream fuel injection, and this effect tends to increase the convective heating. Near the fuel slab leading edge, the effect of boundary-layer growth in the downstream direction dominates the regression rate, but farther downstream, the effect of mass flux becomes more important, thus causing the bowl-shaped regression-rate profiles shown in Fig. 5. In addition, the location of the minimum regression rate $x_{r_{\min}}$ moves downstream with time, as indicated by the heavy line passing through the profiles in the upstream region. It is theorized that because the regression rate is more sensitive to mass flux than to boundary-layer growth, the decrease of mass flux with time tends to favor the boundary-layer growth effect, thus causing the location of minimum regression to move downstream with time. For test 13, $x_{r_{\min}}$ moved about 0.05 x/L (2.9 cm) downstream during the test. The regression rates also vary with position in the downstream region, but generally tend to increase in the downstream direction due to fuel mass addition. The nonuniform regression behavior of the fuel slabs in the downstream region could be caused by the embedded thermocouple extension wires or by surface roughness effects.

The upper portion of Fig. 5 shows the variation of the power n on G, i.e., $r \sim aG^n$, the simplest type of correlation, with time-averaged axial Reynolds number (as measured from the fuel slab leading edge), which has a one-to-one correspondence with the x/L axis. For example, at $x/L = 0.2$, the time-averaged value of Re_x is 2.5×10^5, where Re_x is given on the top horizontal scale. The deduced value of n, obtained by curve fitting a set of instantaneous r values, obtained at a single axial location, with the corresponding set of G values, give an indication of the boundary-layer characteristics. In the downstream region (test 15 data), the particular n at individual axial locations varied slightly, but never departed significantly from the theoretical fully turbulent value of 0.8. In the upstream entrance flow region, however, n shows a much greater dependence on Re_x and xL. Near the slab leading edge for x/L between 0.125 and 0.15, the deduced instantaneous regression rates were independent of G; i.e., $n = 0$. A recirculation zone, caused by incoming GOX flowing around the leading chamfered edges of the fuel slabs, may cause this behavior.

Downstream of this region near the fuel port entrance, the value of n increased approximately linearly until reaching the end of the viewing window at $x/L = 0.28$. This type of behavior suggests that either the flow is not fully developed in the upstream region or that entrance effects influence the flow behavior in this region. It seems that the extent of boundary-layer development should therefore be considered when examining the regression rates because different correlations or parameters may be required to correlate the data in different flow regimes. It is also possible that the boundary layer assumes a laminar profile near the edge of the viewing window in Fig. 5, as indicated by the values of n around 0.6, and then transitions to turbulent flow downstream of this region. However, it is difficult to see how a laminar region could exist in the aggressive environment present in the hybrid motor, especially considering the destabilizing influences of wall blowing and temperature inversion in the boundary layer due to the presence of the flame zone.

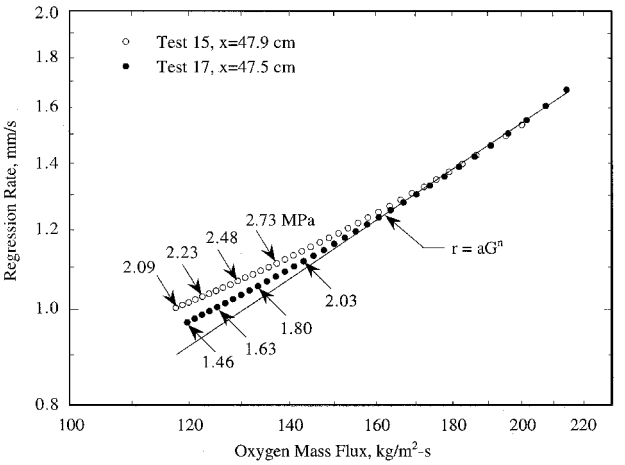

Fig. 6 Effect of thermal radiation on HTPB regression-rate behavior.

Influence of Thermal Radiation

Examining the relationship between regression rate, mass flux, and pressure should help to identify operating condition regimes where either thermal radiation or reaction kinetics influence the regression rate. Figure 6 shows a plot of regression rate vs oxidizer mass flux for tests 15 and 17 at similar axial locations. If convective effects alone govern the regression process, the regression rate should follow a straight line on a log–log plot. However, the regression data for both tests begin to diverge from the convective solution when the mass flux drops below about 140 kg/m^2-s (0.2 lb$_m$/in.^{2}-s). It was surmised that in the lower mass flux regime, the regression data are higher than that predicted by the convective law due to the radiant heat flux to the solid fuel surface from sources such as soot and gas-phase combustion products.

In addition, comparing the regression rates of tests 15 and 17 shows that the influence of radiation on regression rate is more pronounced at higher motor pressures. Even though both tests demonstrated regression rates higher than that predicted by convective theory alone, the test 15 data show higher regression rates in the lower mass flux regime than the data from test 17, which were conducted at the same mass flux but at a lower pressure level. The effect of radiation is not as evident at higher mass fluxes because of the complex interaction of fuel mass blowing, convective heat flux, and radiative heat flux to the fuel surface, but becomes apparent in the low mass flux regime where convection is less dominant. This evidence suggests that some type of radiative model should be included in regression-rate correlations. The increase in regression rate due to radiation in the low-mass flux regime has also been suggested by several other researchers.[12–14] Notice also that the influence of radiation tends to decrease the effective slope of the regression rate vs oxidizer mass flux curve in the low mass-flux regime. The power n of a simple aG_o^n correlation would be lower under the influence of radiation than in the absence of radiation because of the reduced importance of convection (represented by G or G_o). It is interesting to note that several researchers, including Abel et al.,[15] find empirical correlations with relatively low values of n for low-mass flux and high-pressure tests where radiation is expected to be most significant. In Ref. 15, a power of 0.626 was found on G_o for pressures of 500–1100 psi and mass fluxes of 0.025–0.12 lb$_m$/in.^{2}-s. Strand et al.[12] recognized this effect at low flux levels.

The effect of finite rate reaction kinetics, which may act to reduce the regression rate at very high mass fluxes, was not observed in this investigation. According to Lengellé et al.,[16] who tested polyethylene fuels at 3000 kg/m^2-s of air with no noticeable reduction in regression rate, the kinetic effect may not play a significant role for hybrid motors under normal operating pressures.

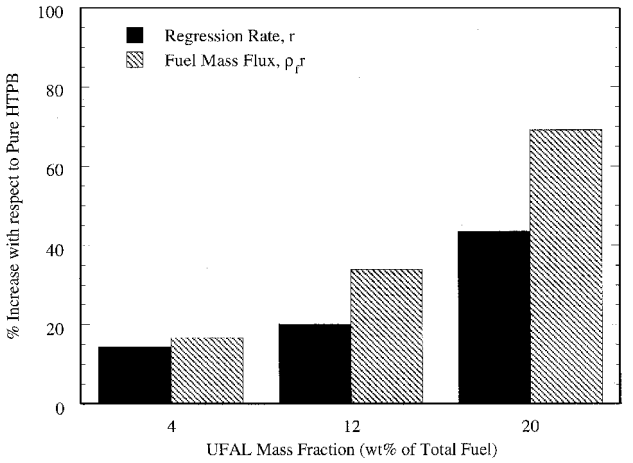

Fig. 7 Effect of UFAL addition on HTPB regression-rate behavior.

Effect of UFAL

As discussed in Ref. 3, the addition of ultra-fine aluminum powder can significantly increase both regression rates and mass burning rates $\rho_f r$ compared with pure HTPB. UFAL powder is manufactured in Russia by exploding thin aluminum wires in an argon environment. The resulting powder has a mean particle size of between 0.05 and 0.10 μm. Figure 7 shows the increase in regression and mass burning rates with weight percent UFAL powder. With a UFAL weight fraction of 20%, the regression rate increased by about 40%, whereas the mass burning rate increased by almost 70%, over that of pure HTPB. This increase is significant because low regression rates are sometimes cited as a drawback of hybrid rocket motors. Based on observations of the different surface structure of recovered slabs of pure HTPB and UFAL-loaded HTPB, the primary mechanism of regression enhancement is thought to be associated with aluminum heat release or particle microexplosion at or near the solid fuel surface.[3] However, the addition of aluminum should also increase the effective radiative heat flux to the fuel surface. These effects are currently under investigation and will be reported in a future paper.

Correlations of Regression Rate with Operating Conditions

The instantaneous regression rate data can be correlated with other instantaneous variables, such as mass flux and motor pressure, to determine their functional relationships. Accurate estimations of solid-fuel regression rates are required for motor design, performance prediction, and minimization of fuel slivers. To correlate experimental data over a broad range of oxidizer flux levels, the effect of gas-phase radiation on regression rate should be considered. The radiative energy flux could be especially important at low oxidizer mass fluxes. Considering an approach similar to that taken by Marxman et al.,[9] who applied a radiative correction to a regression-rate equation based on convection alone, the following functional form was used to correlate instantaneous regression rate with instantaneous motor operating conditions and geometry:

$$r = C_1 G_o^n x^m \left\{ \frac{C_2}{G_o^n x^{n-1}}(1 - e^{-\kappa ph}) + \exp\left[\frac{-C_2}{G_o^n x^{n-1}}(1 - e^{-\kappa ph}) \right] \right\} \tag{1}$$

The dimensionless form of Eq. (1) is:

$$\frac{\rho_f r}{G_o} = a_1 Re_x^{n-1} \left(\frac{x}{L} \right)^{m-n+1} \left\{ \frac{a_2}{G_o Re_x^{n-1}}(1 - e^{-\kappa ph}) + \exp\left[\frac{-a_2}{G_o Re_x^{n-1}}(1 - e^{-\kappa ph}) \right] \right\} \tag{2}$$

The term $(1 - e^{-\kappa ph})$ represents the effective emissivity of the gas phase,[17] whereas the term $C_1 G_o^n x^m$ represents the convective contribution to the regression rate. The long term in curly brackets is a correction factor to account for the influence of thermal radiation on the regression rate. No attempt was made here to separate the radiation of the gas-phase products of combustion (such as CO, CO_2, or H_2O) from those of possible soot particles. Results pertaining to the individual contributions of gas-phase combustion products and soot to the total radiant heat flux will be presented in a future paper. In Eq. (1), when κph is zero, there is no thermal radiation from the gas phase, and the term in curly brackets becomes unity. In the process of correlation development, the data were compared to $C_1 G_o^n x^m$ alone, which was not adequate to account for the regression-rate values at the lower GOX mass fluxes. The more complicated form of Eq. (1) was necessary to accurately correlate the data.

Four separate correlations are presented here: pure HTPB in the upstream region, pure HTPB in the downstream region, 96% HTPB/4% UFAL in the upstream region, and 88% HTPB/12% UFAL in the upstream region. As discussed earlier, the data shown in Fig. 5 suggest that different boundary-layer regimes, namely developing flow and fully developed flow (merged boundary layers), exist in the motor for the operating conditions under investigation for the current study. So far, no instantaneous regression-rate data have been obtained in the hypothesized fully developed regime for UFAL-loaded HTPB. In addition, only a certain axial range, x/L between approximately 0.2 and 0.3, of the regression rate data could be fit using the upstream correlation for both pure and UFAL-loaded HTPB. The regression rate data obtained very near the fuel port entrance have not yet been accurately correlated. It is believed that a more complicated mathematical expression may be required to account for the strong axial variation of n in the entrance region. However, all of the instantaneous regression rate data obtained in the downstream portion of the motor, using the second x-ray viewing window, were fit accurately using the downstream correlation.

For each correlation, the correlation parameters C_1, C_2, m, n, and κ were found using a least-squares analysis to minimize error. Figure 8 shows the experimental regression rate vs the predicted regression rate found using Eq. (1) for pure HTPB. Almost all of the data lie within a ±5% error band, indicating that the correlation properly represents the important physical processes governing solid-fuel regression. However, it should be noted that the data shown in Fig. 8 represent two different correlations: one for the upstream flow region, theorized to have developing boundary layers, and one for the downstream flow region, theorized to have merged boundary layers. The parameters have different values in these two regimes, as shown in Table 3. The value for n in the downstream region is slightly higher than the theoretical value of 0.8. The use of G_o rather than G for the correlation may account for this difference. The n value of 0.5 for the upstream region is coincidentally the same as would be expected for laminar flow; however, as noted earlier, only a portion of the data in the upstream region could be reasonably well fit using Eq. (1). Those data correspond to the downstream portion of the variable n region in the upstream viewing window (around x/L 0.2–0.3 in Fig. 4). The far upstream data have not yet

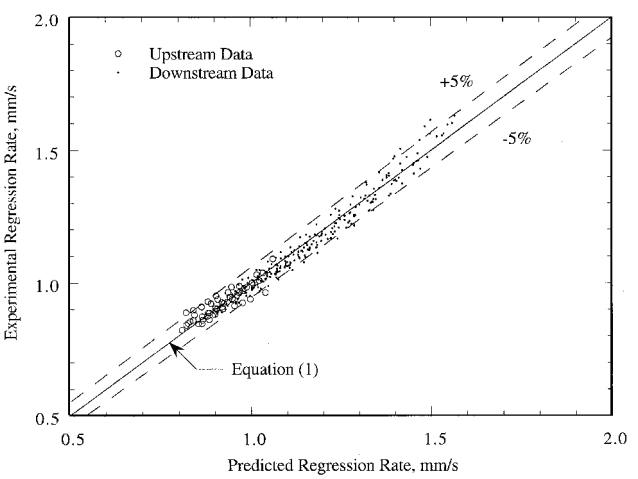

Fig. 8 Regression-rate correlations for pure HTPB.

Table 3 Deduced correlation parameters

Correlation parameter	HTPB		96% HTPB/ 4% UFAL	88% HTPB/ 12% UFAL
	Upstream	Downstream		
C_1	0.1165	0.0158	0.0535	0.2538
C_2	6.632	84.389	14.197	14.197
n	0.50	0.90	0.63	0.63
m	0.313	0.344	0.122	0.882
k	17.13	17.13	57.11	57.11

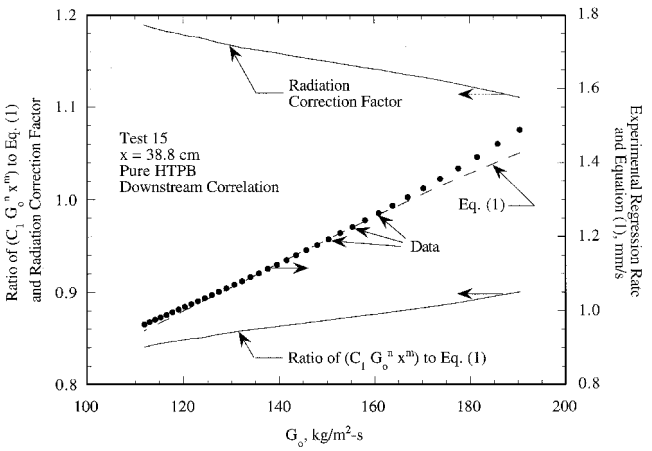

Fig. 9 Radiative and convective contributions to HTPB regression rate.

been satisfactorily correlated, and it is believed that the developing boundary-layer region may require a more complex form than that given by Eq. (1) to account for entrance flow and developing boundary-layer effects.

In contrast to convective regression-rate theory, a positive power on the axial location variable x was necessary to correlate the regression-rate data. According to convective theory, the regression rate should depend on axial position x to the -0.2 power for turbulent flow. Here, an overall positive power on x was found for all correlations. Because G_o has been used here instead of G, the positive power on x may account for the increase in regression rate due to mass accumulation in the downstream direction. An additional explanation for the differences between the values of theoretical and experimental correlation parameters may involve the confined nature of the flow. Theoretical treatments of regression-rate behavior usually involve skin friction or heat transfer correlations for turbulent flow over a flat plate in external flow. However, practical hybrid rocket combustion occurs in internal flow along a fuel port. In this situation, acceleration of the core flow due to heat and mass addition in the downstream direction, velocity profile distortion due to the presence of the flame in the boundary layer, and extent of flow development may also affect the regression-rate internal ballistics.

Figure 9 illustrates several features of the downstream correlation for pure HTPB for test 15 at an axial location 38.8 cm downstream from the front edge of the fuel slabs. The left vertical axis shows both the radiation correction factor [the term in curly brackets on the right side of Eq. (1)] and the ratio of $C_1 G_o^n x^m$ to the total correlation, Eq. (1). The right vertical axis shows both the experimental regression-rate data and the regression-rate correlation. Compared to the regression-rate data, the correlation is quite accurate over the entire oxidizer mass flux range, diverging by a maximum of about 5% at the higher mass flux regime. At the upper end of the mass flux range, the ratio of $C_1 G_o^n x^m$ to the correlation is about 90%, indicating that the convective term accounts for about 90% of the overall value of the correlation. However, at the lower end of the mass flux range, convection accounts for about 84% of the overall correlation. On the other hand, thermal radiation becomes relatively more important as mass flux decreases. The radiation correction factor has a value of 1.11 at an oxidizer mass flux of 190 kg/m^2-s and increases to a value of 1.19 at an oxidizer mass flux of 112 kg/m^2-s, showing that radiation has a relatively stronger effect at lower mass fluxes due to weaker convective heat transfer. Of course, these particular radiation correction values also depend on the motor pressure and the port height, in accordance with Eq. (1). At G_o of 190 kg/m^2-s, the pressure and port height were 4.9 MPa (712 psi) and 1.64 cm, respectively, whereas at 112 kg/m^2-s, the p and h were 2.09 MPa (303 psi) and 2.73 cm. Severe erosion of the graphite nozzle caused the motor pressure to drop 2.81 MPa (409 psi) in about 5 s during this test. At higher pressures, the radiative contribution should be even more prominent in the lower mass flux regime. Reference 5 presents detailed chamber pressure results for the motor used in this study.

Separate correlations were developed for the 96% HTPB/4% UFAL and 88% HTPB/12% UFAL fuel formulations in the upstream region. Table 3 lists the parameters for these correlations, which also had an error of ±5% with respect to the experimental data. Similar values were obtained for most of the parameters, but the 12% UFAL fuel formulation showed a greater dependence on axial location, as shown by the higher m value. Because the 12% UFAL slab had a substantially higher fuel mass flux than the 4% UFAL sample, the boundary layer may undergo more rapid growth in this case, leading to a stronger dependence on axial location.

The value of κ was higher for the UFAL fuel formulations than for the pure HTPB cases. This result is expected for metal-loaded fuels that should show a greater dependence on radiation due to higher gas-phase emissivity from vaporized metal particles.

Solid-Fuel Temperature Results

Like the regression rate, the pyrolyzing surface temperature is an important variable in the study of solid-fuel pyrolysis behavior. The surface temperature can provide information on solid-fuel degradation processes, pyrolysis kinetics, and heat flux conducted into the subsurface region of the fuel grain. Figure 10 shows a pair of typical fuel temperature measurements from test 7, which had an initial GOX mass flux of 102 kg/m^2-s. The profile in the downstream location at 52.1 cm shows a higher surface temperature of 1020 K and thinner thermal wave than does the upstream profile at 6.4 cm, which had a lower deduced surface temperature of 930 K, due to higher convective heat fluxes caused by increased mass flux in the downstream direction.

Figure 11 shows the effect of different operating conditions on temperature characteristics. Test 6 (initial GOX flux of 133 kg/m^2-s)

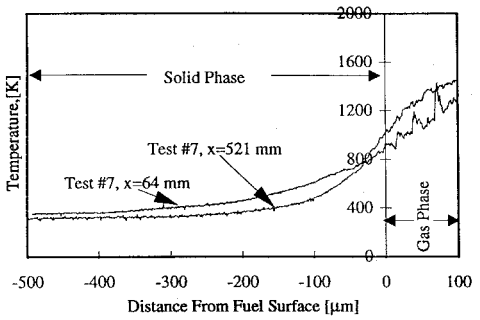

Fig. 10 HTPB fuel temperature profiles from test 7.

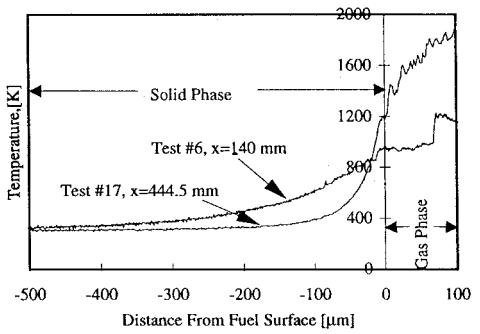

Fig. 11 HTPB fuel temperature profiles from tests 6 and 17.

had a deduced surface temperature of 970 K and a thermal wave about 0.64 mm thick, whereas test 17 (initial GOX flux of 370 kg/m^2-s), had a higher surface temperature of about 1190 K and a thinner thermal wave of about 0.32 mm. Here, the thermal wave is defined as the depth below the fuel surface where the temperature has dropped from the surface temperature value to 1% above the initial fuel temperature. The thinner thermal wave of test 17 implies a higher heat flux to the fuel surface due to the larger injected GOX mass flux. It should also be noted that the 25-μm thermocouple junction is a nontrivial fraction of the thermal wave thickness for test 17. This situation may cause some error in the fuel temperature measurement.

Solid-Fuel Arrhenius Law

A solid-fuel pyrolysis law was obtained by relating the regression rate to the surface temperature through the Arrhenius equation:

$$\rho_f r = A \exp \frac{-E_a}{2R_u T_s} \tag{3}$$

Figure 12 compares the results of several studies on an Arrhenius-type plot of the solid-fuel mass flux $\rho_f r$ vs reciprocal surface temperature $1/T_s$. In general, the PSU data match quite well with those found in previous studies and fall within the range of error suggested by Cohen.[18] The differences with the law from Ref. 16 may be due to the different methods used to determine the surface temperature and variations in the specific HTPB formulation. For instance, Cohen et al. used R-45 prepolymer, isodecyl pelargonate plasticizer, toluene-2, 4-diisocyanate curative, and 3% carbon black,[18] whereas Arisawa and Brill[19] performed their experiments on uncured R-45M. The pyrolysis data from Ref. 18, used in Ref. 16, were extrapolated from differential scanning calorimetry experimental data with low heating rates on the order of 0.2 K/s for a surface temperature around 700 K to the heating rates for hybrid motor conditions (on the order of 1500 K/s) and a surface temperature of about 1000 K. Lengellé et al.[16] recognized this rather long extrapolation.

As indicated by Eq. (3), a least-squares fit of $\ln(\rho_f r)$ vs $1/T_s$ provides an estimate of the activation energy E_a and pre-exponential constant A, for HTPB pyrolysis. The slope of the curve in Fig. 12 is -2891 K, which, when multiplied by $2R_u$, gives a value of 11.5 kcal/mole for E_a. This value is quite similar to that of 12 kcal/mole given by Arisawa and Brill[19] for the overall activation energy of HTPB under high heating rates. Cohen et al.[18] found an E_a value of 16.9 kcal/mole. Relatively low-activation energies such as those stated earlier indicate that the overall regression process is limited by physical desorption of high-molecular-weight fuel fragments from the surface rather than by bulk-phase chemical processes. The latter process is characterized by higher activation energies on the order of 50 kcal/mole,[19] and dominate the regression action at low heating rates and surface temperatures.

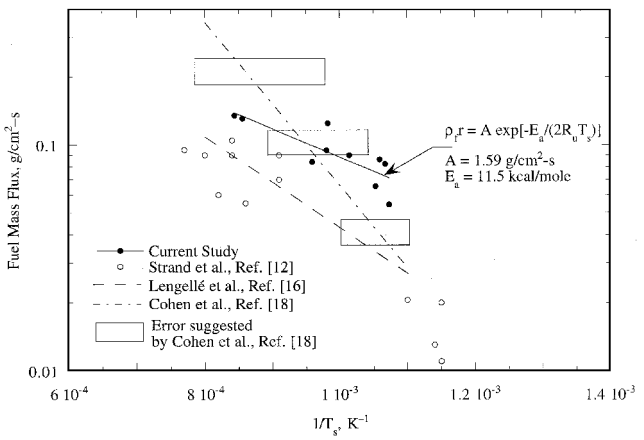

Fig. 12 Comparison of several HTPB fuel pyrolysis studies.

Conclusions

Several conclusions can be drawn from the results of this investigation:

1) Near the motor head-end, the regression rates were observed to decrease with axial location until a location of minimum regression rate was reached. Beyond this point, the regression rates generally increased with axial location due to fuel mass flux addition. The existence of minimum regression rate results from the competition between boundary-layer growth and local mass flux. The internal ballistic results also suggest that the regression rates may be sensitive to whether or not the boundary layers have merged. In addition, a recirculation zone may exist near the fuel port inlet that causes a zone of flux-independent regression.

2) The solid-fuel regression rate was influenced in a nonnegligible amount by thermal radiation. This effect is more pronounced at lower mass fluxes and higher chamber pressures.

3) The addition of UFAL powder caused a significant increase in the solid-fuel regression rate. With the addition of 20% by weight UFAL (the maximum amount tested), the fuel mass flux increased by 70% over that of pure HTPB. The primary mechanism of regression enhancement is thought to be associated with particle energy release near the solid-fuel surface. However, the addition of UFAL also increases the radiant flux to the fuel surface.

4) Taking into account the effects of boundary-layer development, axial location, thermal radiation, and fuel formulation, semi-empirical correlations were developed to describe the regression rate of HTPB as a function of oxidizer mass flux, motor pressure, axial location, and port height. Though scaling effects have not yet been considered, it is believed that these correlations may prove useful for motor performance prediction and efficient fuel grain design.

5) The burning-surface temperature of pure HTPB varied from 930 to 1190 K, depending on operating conditions. For a given test, the downstream locations tended to display higher surface temperatures and thinner thermal waves due to higher heat transfer rates.

6) The activation energy of HTPB was estimated at 11.5 kcal/mole. This value suggests that, for the high heating rates and temperatures characteristic of practical hybrid rocket motors, the overall fuel-regression process is governed by desorption of high-molecular weight fragments from the solid-fuel surface rather than bulk-phase chemical processes.

Acknowledgments

This work was conducted under a gift fund to PSU. The authors would like to thank Roger Harwell of NASA Marshall Space Flight Center, and Marion D. Kitchens of NASA Headquarters, for funding the initial portion of the research. We would also like to thank Les Tepe of the Phillips Lab, and David M. Mann of the Army Research Office, for supporting the purchase of the Ultrasonic Measurement System from ONERA, France prior to this investigation. Under sponsorship from NATO/AGARD, the help of Franck Cauty of ONERA in the technology transfer of the ultrasonic pulse-echo technique to PSU research team is greatly appreciated. The authors also wish to thank the Scientific and Technical Research Council of Turkey for sponsoring the scholarship of Nadir Serin, which enabled his participation in this study.

References

[1] "A Short Course on the Concepts, Systems, Applications, and Operating Principles of Hybrid Rockets," AIAA Hybrid Rocket Technical Committee, Washington, DC, July 1995.

[2] Boardman, T. A., Carpenter, R. L., Goldberg, B. E., and Shaeffer, C. W., "Development and Testing of 11- and 24-Inch Hybrid Motors Under the Joint Government/Industry IR&D Program," AIAA Paper 93-2552, June 1993.

[3] Chiaverini, M. J., Serin, N., Johnson, D. K., Lu, Y. C., and Kuo, K. K., "Instantaneous Regression Behavior of HTPB Solid Fuels Burning with GOX in a Simulated Hybrid Rocket Motor," *Proceedings of the 4th International Symposium on Special Topics in Chemical Propulsion*, Begell House, New York, 1997, pp. 719–733.

[4] Chiaverini, M. J., Harting, G. C., Lu, Y. C., Kuo, K. K., Serin, N., and Johnson, D. K., "Fuel Decomposition and Boundary-Layer Combustion Processes of Hybrid Rocket Motors," AIAA Paper 95-2686, July 1995.

[5]Chiaverini, M. J., Harting, G. C., Lu, Y. C., Kuo, K. K., Serin, N., and Johnson, D. K., "Combustion of Solid Fuel Slabs with Gaseous Oxygen in a Hybrid Motor Analog," *32nd JANNAF Combustion Meeting*, CPIA Pub. 631, Vol. 1, Huntsville, AL, Oct. 1995, pp. 135–148.

[6]Cauty, F., Demarais, J. C., and Erades, C., "Determination of Solid Propellant Burning Rate Sensitivity to the Initial Temperature by the Ultrasonic Method," *Non-Intrusive Combustion Diagnostics*, edited by K. K. Kuo and T. P. Parr, Begell House, New York, 1994, pp. 642–653.

[7]Kuo, K. K., and Parr, T. P. (eds.), *Non-Intrusive Combustion Diagnostics*, Begell House, New York, 1994, pp. 365–423.

[8]Shanks, R. B., and Hudson, M. K., "The Design and Control of a Labscale Hybrid Rocket Facility for Spectroscopy Studies," AIAA Paper 94-3016, June 1994.

[9]Marxman, G. A., Wooldridge, C. E., and Muzzy, R. J., 1964. "Fundamentals of Hybrid Boundary Layer Combustion," *Heterogeneous Combustion*, Progress in Astronautics and Aeronautics, edited by H. G. Wolfhard, I. Glassman, and L. Green Jr., Vol. 15, AIAA, New York, 1964, pp. 485–521.

[10]Sutton, G., *Rocket Propulsion Elements: An Introduction to the Engineering of Rockets*, 6th ed., Wiley, New York, 1992, pp. 512, 513.

[11]Marxman, G. A., and Gilbert, M., "Turbulent Boundary Layer Combustion in the Hybrid Rocket," *9th International Symposium on Combustion*, Academic, New York, 1963, pp. 371–383.

[12]Strand, L., Jones, M. D., Ray, R. L., and Cohen, N. S., "Characterization of Hybrid Rocket Internal Heat Flux and HTPB Fuel Pyrolysis," AIAA Paper 94-2876, June 1994.

[13]Estey, P. N., Altman, D., and McFarlane, J. S., "An Evaluation of Scaling Effects for Hybrid Rocket Motors," AIAA Paper 91-2517, June 1991.

[14]Muzzy, R. J., "Applied Hybrid Combustion Theory," AIAA Paper 72-1143, Nov. 1972.

[15]Abel, T. M., Carpenter, R. L., Claflin, S. A., Crawford, J. T., and Holt, D. M., "SRM Simulation and Hybrid Propulsion Testing at the Marshall Space Flight Center," AIAA Paper 95-2944, July 1995.

[16]Lengellé, G., Fourest, B., Godon, J. C., and Guin, C., "Condensed Phase Behavior and Ablation Rate of Fuels for Hybrid Propulsion," AIAA Paper 93-2413, June 1993.

[17]Incropera, F. P., and DeWitt, D. P., *Fundamentals of Heat and Mass Transfer*, 3rd ed., Wiley, New York, 1990, pp. 872–833.

[18]Cohen, N. S., Fleming, R. W., and Derr, R. L., "Role of Binders in Solid Propellant Combustion," *AIAA Journal*, Vol. 12, No. 2, 1974, pp. 212–218.

[19]Arisawa, H., and Brill, T. B., "Flash Pyrolysis of Hydroxyl-Terminated Polybutadiene (HTPB) II: Implications of the Kinetics to Combustion of Organic Polymers," *Combustion and Flame*, Vol. 106, No. 1, 2, 1996, pp. 144–154.